

Layered Droplet Microstructures in Sheared Emulsions: Finite-Size Effects

Jai A. Pathak,¹ Melissa C. Davis,² Steven D. Hudson,¹ and Kalman B. Migler¹

National Institute of Standards and Technology, Polymers Division, 100 Bureau Drive, Gaithersburg, Maryland 20899-8544

Received January 9, 2002; accepted July 15, 2002

We investigate the influence of confinement on the steady state microstructure of emulsions sheared between parallel plates, in a regime where the average droplet dimension is comparable to the gap width between the confining walls. Utilizing droplet velocimetry, we find that the droplets can organize into discrete layers under the influence of shear. The number of layers decreases from two (at relatively higher shear rates) to one (at lower shear rates), as the drops grow slightly larger due to coalescence. We argue that the layering and overall composition profile may be controlled by the interplay of droplet collisions (which can cause separation of droplet centers in the velocity gradient direction), droplet migration toward the centerline (due to wall effects), and droplet packing constraints. We also study the effects of mixture composition on droplet microstructure, and summarize these results in the form of a morphology diagram in the parameter space of mass fraction and shear rate. We find that formation of strings of the suspended phase (reported earlier by our group in flow-visualization studies on confined emulsions) is observed over a broad composition window. We also find a stable (nontransient) morphology wherein the droplets are arranged in highly ordered pearl-necklace chain structures. © 2002 Elsevier Science (USA)

Key Words: emulsions; finite-size effects; confinement; wall migration; collisions; layering.

INTRODUCTION

Most studies on emulsion rheology have focused on systems where the average droplet radius (r) is much smaller than the gap (d) between the confining walls (e.g., parallel plates or the concentric cylinders forming the annulus of a Couette cell). The regime where r and d are comparable, where wall effects (1) on droplet motion are crucial, is poorly understood, making this problem important from the scientific perspective. It is also technologically attractive, given the recent explosion in research on microfluidics (2, 3) and the potential for microscale processing of emulsions. Migler (4) has recently reported the

formation of strings in polymeric emulsions composed of polyisobutylene (PIB) and poly(dimethylsiloxane) (PDMS), sheared between parallel plates in the regime where $r \approx d$. The strings observed in these emulsions are formed by the coalescence of droplets of the suspended phase. The essential physics behind the transition from the droplet to string morphology is governed by the ratio r/d . In the regime where $r \approx d$, strings are formed when the droplets have grown sufficiently large due to coalescence. In the regime $r \ll d$, “bulk” behavior (whose metric will be defined shortly) of droplets in a matrix is observed.

Our fundamental understanding of emulsion rheology stems from the seminal experimental and theoretical work of G. I. Taylor on droplet deformation and breakup (5, 6) in the 1930s. Much effort has since been directed toward the study of the effect of deformation on the shape of emulsion droplets in flow fields (7–9). A fluid droplet dispersed in another immiscible fluid is spherical at rest. When a shear field is imposed on an emulsion, interfacial tension effects tend to keep the droplet spherical, while shear stress acts to deform it. The droplet continues to deform until the interfacial tension effects can no longer balance the shear-stress-induced deformation and then the droplet breaks up. These effects are quantified by the dimensionless capillary number, $Ca = \frac{\eta_m \dot{\gamma} r}{\sigma}$, where η_m denotes the matrix viscosity, $\dot{\gamma}$ is the shear rate, r is the droplet radius, and σ is the interfacial tension. Above a certain value of Ca (which is a function of the viscosity ratio, $\lambda = \frac{\eta_d}{\eta_m}$; η_d is the droplet viscosity), the droplet is unstable, and the corresponding Ca is known as the critical capillary number, Ca_c . Taylor quantified droplet deformation (D) as $D = \frac{L-B}{L+B}$, where L and B are the major and minor axes of the drop, respectively. He predicted that D depends linearly on Ca : $D = Ca \cdot F(\lambda)$, in the limit of small deformation, where $F(\lambda) = \frac{19\lambda + 16}{16(\lambda + 1)}$. Taylor’s theory is derived for a *single droplet*. Another phenomenon, droplet coalescence, occurs in addition to droplet breakup in concentrated emulsions, whereby small droplets fuse together to form larger ones. Chesters has provided a review of flow-driven collision and coalescence in liquid–liquid dispersions (10). The major issues related to coalescence phenomena are nicely discussed in the Introduction section of a recent paper by Yang *et al.* (11). Coalescence and breakup occur *simultaneously* in concentrated emulsions, leading to a statistical distribution of drop

¹ To whom correspondence should be addressed. E-mail: Jai.Pathak@nist.gov, Steven.Hudson@nist.gov, Kalman.Migler@nist.gov.

² Permanent address: Chemical Engineering Department, University of California—Irvine, Irvine, CA 92697.

sizes, which naturally results in a distribution of Ca for these systems.

The newly discovered string formation phenomenon in the regime where $r \approx d$ offers potential for experimental investigation, given the rich parameter space that governs emulsion rheology (12). These factors include the mixture composition, the viscosity ratio, the component density ratio, the elasticity of the component fluids, the presence of a surfactant in the emulsion, etc. In this study, λ is fixed to a value close to 1. The study of Migler (4) was limited to one composition (mass fraction PDMS = 28%) and his work focused on string formation. To study the influence of composition on *steady-state* droplet morphology observed in the transition from bulk-like behavior of droplets to strings in the confined emulsion, we varied the mass fraction of the components in the mixture. We discuss the results in the form of a morphology diagram, wherein we depict the microstructure pathway of the transition from droplets to strings in the parameter space of mass fraction and shear rate. Video shear microscopy data on PDMS/PIB blends seem to indicate that the droplets move in discrete layers in the regime where $r \approx d$. To quantify these effects, we have measured the droplet velocity distributions. At some shear rates, there exist two modes in the velocity distribution, and the number of modes is a function of composition and shear rate. We associate each mode with the existence of a layer of droplets.

After extracting droplet velocity distributions and collision rates from experimental data, we offer some arguments on the physics behind the persistence of droplet layers in these confined systems. We also calculate the collision frequency in a *layered* system and find that it reasonably describes the dependence of the experimentally measured collision frequency on shear rate. By comparing the appropriate time scales for droplet collision and droplet migration away from the walls, in conjunction with finite-size effects, we illustrate how the “stability” of the two-layer state may be governed by the interplay of these factors.

The formation of particle layers has been observed by Ackerson *et al.* (13, 14), by *in situ* shear light scattering in concentrated hard-sphere suspensions. They established layering by constructing a real space arrangement of particles from reciprocal space diffraction patterns. The arrangement of particles into well-defined layers was ascribed by Ackerson *et al.* to the tendency to minimize the energy dissipated by particle collisions in the suspension (15).

Our velocity calculations are based on *direct* visualization of the emulsion in real space, so that there is no uncertainty about the nature of the phenomenon. Our results of a layered structure of concentration profiles in linear flow fields are in contrast to those of prior reports (16, 17) of peaks in the concentration profile adjacent to drop free zones at the wall, which represent either transient profiles or more complex migration in quadratic flow fields. Droplet interactions and collisions were also considered negligible in that study, in contrast to this work.

EXPERIMENTAL

Materials, Rheological Characterization, and Emulsion Preparation

Both the PIB (mass average molecular mass, $M_w = 800$; PolySciences³) and PDMS ($M_w = 62,700$; Gelest) samples used here have zero shear viscosities $\eta_0 = 10 \text{ Pa} \cdot \text{s}$ at 25°C (see Fig. 1), yielding $\lambda = 1$. The standard uncertainty associated with the measured viscosity is $0.2 \text{ Pa} \cdot \text{s}$. The entanglement molecular weights of PIB and PDMS at 25°C are 7000 and 15,000, respectively (18). We can expect the unentangled pure PIB chains to be Newtonian at all accessible shear rates. The pure component and emulsion rheology was measured on a Rheometric Scientific ARES rheometer equipped with a Force Rebalance Transducer, using 25-mm cone-and-plate fixtures. A viscosity standard (Brookfield) with $\eta = 0.95 \text{ Pa} \cdot \text{s}$ (25°C) was used to calibrate ARES. Between $\dot{\gamma} = 0.1 \text{ s}^{-1}$ and $\dot{\gamma} = 10 \text{ s}^{-1}$, the viscosity of both pure components was independent of shear rate and the first normal stress difference was too small to be reliably measured by the normal force transducer in ARES. The pure components behave as well-defined Newtonian liquids under these conditions. It is shown later that the density difference between PIB and PDMS is small enough so that gravitational effects are negligible ($\rho_{\text{PIB}} = 890 \text{ kg/m}^3$ at 20°C and $\rho_{\text{PDMS}} = 970 \text{ kg/m}^3$ at 20°C (19); droplet to matrix density ratio, $\kappa = 1.08$). The value of σ for the PDMS/PIB system is known to be $2.5 \times 10^{-3} \text{ N/m}$ (20).

Only PIB rich blends are discussed here. Six compositions (1, 5, 10, 20, 28, and 35% mass fraction PDMS) were investigated in this work. All compositions referred to henceforth in this publication refer to mass fraction of PDMS. The mixtures were prepared by weighing the components into glass jars and then stirring them gently (to avoid chain scission and to create a uniform dispersion) with a spatula. Trapped air bubbles were removed by leaving the emulsions overnight under vacuum at ambient temperature. No separation or sedimentation was observed while the emulsions were stored overnight.

Experimental Apparatus and Procedure

All shear microscopy experiments were performed in a Linkam CSS-450 commercial shear cell, consisting of two parallel quartz plates (diameters of the upper and lower plates are 30 and 40 mm, respectively). The bottom plate is connected to a dynamic motor capable of both steady and oscillatory shear, and the gap width between the plates is adjusted by a stepper motor. The gap width was consistently set to $36 \mu\text{m}$ in this study, the smallest gap width studied by Migler (4). The circular

³ Certain commercial materials and equipment are identified in this paper in order to adequately specify the experimental procedure. In no case does such identification imply recommendation or endorsement by the National Institute of Standards and Technology, nor does it imply that these are necessarily the best available for the purpose.

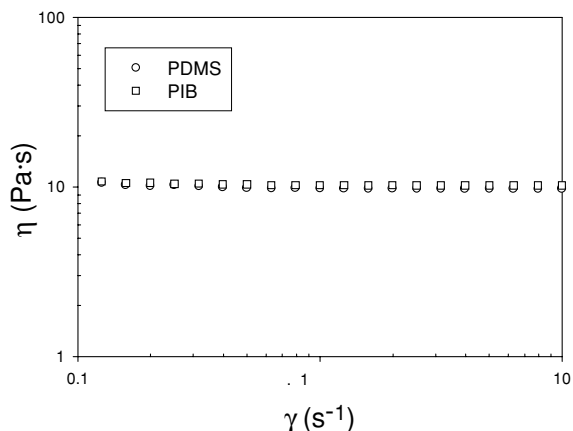


FIG. 1. Shear viscosities, $\eta(\dot{\gamma})$, of PIB and PDMS.

observation window (diameter = 2.5 mm) on the top plate is located at a distance of 7.5 mm from the center. The shear cell, incorporated into an optical microscope (Carl Zeiss), is interfaced with a PC that controls the gap setting, shear rate, and temperature. Objectives of 3.5X, 10X, and 40X magnification were used. Images were acquired by an analog video camera (Pulnix TM-9701) and recorded on S-VHS videotape on a VCR interfaced with a video stopwatch (Horita VS 50).

All experiments (only steady shear experiments) were performed at $25 \pm 1^\circ\text{C}$. The Reynolds number, $Re = \frac{\rho \dot{\gamma} r^2}{\eta_m}$, is very small; $Re \sim O(10^{-8})$, and so Stokes flow prevails. The experimental procedure involved a step down in shear rate using small decrements. All experiments were performed at shear rates that correspond to Ca approximately 0.2 at steady state. At each shear rate data were acquired after shearing for at least 2 h. After that, the shear rate was decreased and data were acquired at the new shear rate, as described. All images were acquired in the velocity–vorticity plane, enabling determination of droplet dimensions in the velocity and vorticity directions, along with droplet velocities. In some cases, after steady state was reached at each shear rate, the flow was temporarily stopped for a few seconds and the droplets were allowed to relax back from ellipsoids to spheres. By equating the volume of the sphere to the volume of the equivalent ellipsoid, the droplet dimension in the velocity gradient direction was calculated. Due care was taken to ensure that no coalesced particles were considered in this analysis. Finally, the reproducibility of the data has been verified by repeating experiments on a few randomly chosen compositions and then performing droplet velocimetry (discussed next) to ensure that for any given composition at any given shear rate the velocimetry results give reproducible results.

Data Analysis

The recorded images were analyzed to quantify the velocity of the droplets in the sheared emulsions. All droplets in each frame were first identified manually and the velocity of each individual

droplet was then calculated by determining the time taken by it to travel a fixed distance. For velocity calculations, typically 80 to 100 drops were analyzed. In addition, the number of collisions per unit time experienced by droplets was also calculated from experimental data to determine the collision frequency. A “collision” was defined to occur when two droplets flowed immediately past each other (21). A droplet was picked at random from the ensemble, and the number of unique *nearest* neighbor droplets (within a distance approximately equal to the average droplet radius) it flowed past, over a given time interval, was used to determine the collision rate per unit time for that droplet. An average of at least 50 drops was used for each data point. Droplet sizes were quantified by means of National Instruments IMAQ Vision Builder Software (v. 5.0). Spatial calibration was done with the help of a Ronchi grating (Rolyn Optics) having 39.37 cycles/mm.

RESULTS

Finite-Size Effects and Droplet Dimensions

We first discuss the velocity distributions. Between $\dot{\gamma} = 8.5 \text{ s}^{-1}$ and $\dot{\gamma} = 5.25 \text{ s}^{-1}$, the velocity distribution in a 20% PDMS/PIB emulsion is clearly *bimodal* (see Figs. 2a–2e), signifying that the droplets are moving in two layers. Similar results have been inferred in passing by Zhou and Pozrikidis (22) in their 2D computer simulations on emulsions in confined simple shear flows. In their analysis of the stability of the one-layer state, double-file (two-layer) states were sometimes found to be stable. For an *isolated* droplet, the velocity profile is linear, enabling ready assignment of droplet location from its velocity. The velocity profile in concentrated emulsions is nonlinear (23). The center of a drop, which is traveling with a velocity $v_{\text{max}}/3$, will *not* lie at a distance $d/3$ from the stationary plate. In concentrated emulsions, only the locations of the minimum and maximum velocities $v_{\text{min}} = 0$ and $v_{\text{max}} = \dot{\gamma}d$ (dictated by no-slip conditions for the matrix fluid at the stationary and steadily rotating plates, respectively) and the centerline velocity $0.5 v_{\text{max}}$ (due to symmetrical effects from each wall) are unambiguously known. Thus, a trivial consequence of two modes would be two peaks in the concentration profile (as a function of position between the bounding surfaces). This result may be contrasted with the histograms shown by King and Leighton (24), where *only one peak* is seen in the volume fraction profile, under all conditions. The r/d ratio for their system is $\ll 1$ (see Table 1 in Ref. 24), suggesting that the formation of droplet layers is a finite-size effect (gravitational effects are negligible here; see “Discussion”). At $\dot{\gamma} = 4.25 \text{ s}^{-1}$ (Fig. 2f), the histogram shows a single mode but a rather broad distribution of velocities, signifying that the transition from the two layer to the one layer state has begun. Below $\dot{\gamma} = 4.25 \text{ s}^{-1}$ (Figs. 2g and 2h), only one sharp mode is seen in the histograms. The obvious consequence of a single mode roughly halfway between the plates is that most droplets have migrated close to the center. When only one mode exists,

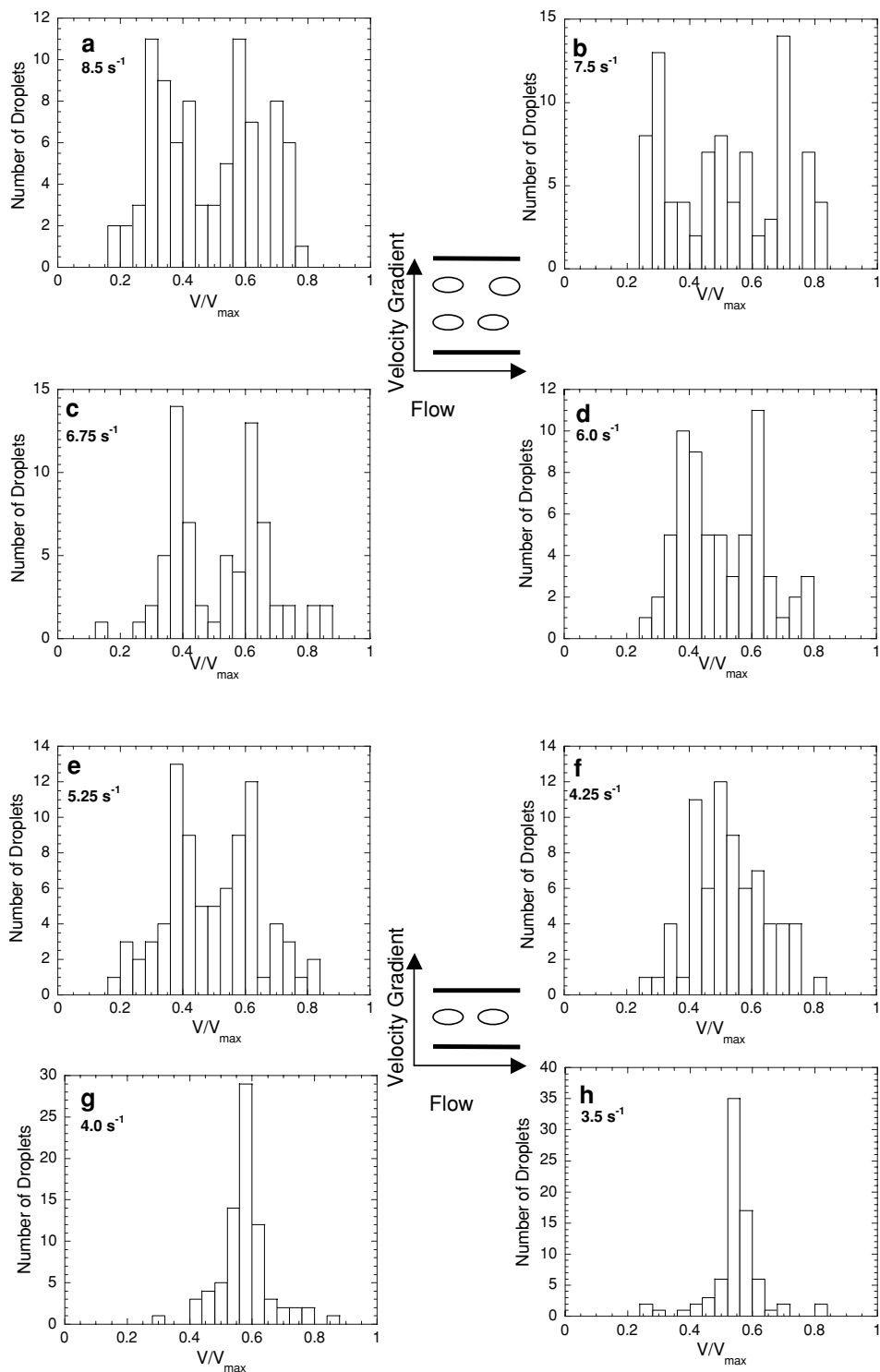


FIG. 2. Typical histograms of the velocity (v) distribution in a 20% PDMS/PIB emulsion at (a) $\dot{\gamma} = 8.5 \text{ s}^{-1}$, (b) 7.5 s^{-1} , (c) 6.75 s^{-1} , (d) 6.0 s^{-1} , (e) 5.25 s^{-1} , (f) 4.25 s^{-1} , (g) 4.0 s^{-1} , and (h) 3.5 s^{-1} . The velocity of the top plate is denoted by v_{max} . The sketches denote the droplet arrangement in the layered states.

comparison of the velocity distribution width, δ , and r may be used to classify the system either as “bulk” (cf. King and Leighton (24), where $\delta/(r\dot{\gamma}) > 1$) or as a single layer of drops, as is discerned in Fig. 3, where $\delta/(r\dot{\gamma}) < 1$.

To elucidate the role of finite-size effects, we compare the droplet dimension in the velocity gradient direction (the direction of confinement) with the gap width between the parallel plates. The size in the velocity gradient direction was determined

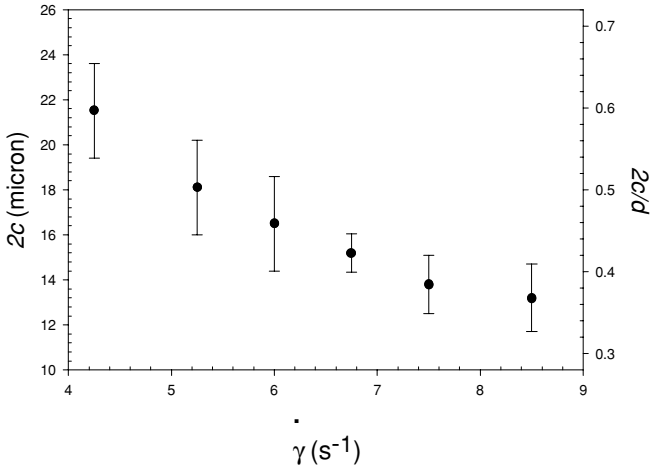


FIG. 3. Droplet dimension, $2c$, in the velocity gradient direction versus $\dot{\gamma}$ for the 20% PDMS/PIB emulsion. Dimensionless droplet size, $2c/d$, is plotted with respect to the right ordinate axis. The bar on each data point reflects the standard uncertainty (in this case, the standard deviation) associated with the point.

for the 20% PDMS emulsion at different shear rates (see Fig. 3). At $\dot{\gamma} = 8.5 \text{ s}^{-1}$ (where the histogram indicates two layers of droplets) the average droplet dimension ($2c$) in the velocity gradient direction = $13.2 \mu\text{m}$ ($d = 36 \mu\text{m}$).⁴ This is consistent with the observation of two layers of droplets in the system, as no more than two layers of droplets of this size can be packed between the plates. The droplet size grows with decreasing shear rate due to coalescence, and at $\dot{\gamma} = 6.0 \text{ s}^{-1}$, $2c = 16.5 \mu\text{m}$, also consistent with two layers. However, at $\dot{\gamma} = 4.25 \text{ s}^{-1}$ (where only one mode is seen in the velocity histogram), $2c = 21.5 \mu\text{m}$. With $d = 36 \mu\text{m}$, it is certainly not possible to pack more than one layer of droplets between the plates. Thus, finite-size effects are important for determining the shear rate where the *transition* from a two-layer to a one-layer arrangement of droplets occurs.

Since we have determined droplet dimensions in the velocity gradient direction and since the confinement in this problem is in the gradient direction, we compare our data to the prediction of the quadratic theory of Rallison (25) for shear-induced deformation of a single viscous droplet in the low Re and small deformation regime.

$$\frac{c}{r} = 1 - 3CaF_{xy} + Ca^2 \left[-\frac{12}{5}F_{xy}^2 - \frac{3}{2}L_{zz} + \frac{1995}{4}M_{zzzz} \right] \quad [1]$$

Here c denotes the smaller principal axis of the drop lying in the plane perpendicular to the vorticity axis. Here, $F_{xy} = f/2$, $L_{zz} = -\eta/6$ and $M_{zzzz} = 3\mu/35$, while f , η , and μ are defined

⁴ This calculation is based on the assumption that the major axis of the drop is parallel to the flow, i.e., the inclination angle is zero. Assuming an inclination angle greater than zero causes the calculated magnitude of the principal axis to decrease. A value of approximately 17° for the inclination angle yields a best fit with Rallison's theory (25) (cf. Fig. 4). Somewhat larger values are predicted for unconfined drops (38, 26).

below.

$$f = \frac{19\lambda + 16}{24(\lambda + 1)}$$

$$\eta = \frac{11419\lambda^3 + 26583\lambda^2 + 19152\lambda + 4096}{3360(1 + \lambda)^3} \quad [2]$$

$$\mu = \frac{28538\lambda^4 + 120305\lambda^3 + 186883\lambda^2 + 126496\lambda + 31488}{544320(3 + 2\lambda)(1 + \lambda)^3}$$

The Rallison theory shows reasonable agreement with the data, i.e., the prediction certainly lies within the uncertainty associated with the data points (see Fig. 4). Note that Ca weakly changes with $\dot{\gamma}$, since we are in the regime where $r \sim \dot{\gamma}^{-0.66}$ (instead of $r \sim \dot{\gamma}^{-1.0}$). Admittedly, this is not a stringent test of the theory as the Ca range covered here is small and the value of the inclination angle is uncertain. However, agreement between theory and experiment is somewhat surprising, since the theory was developed for an isolated droplet. In the isolated droplet case, Guido and Greco (26) have shown that the Rallison theory makes quantitative predictions for the deformed droplet dimensions and the droplet relaxation to spherical shape after cessation of steady shear. This simple exercise demonstrates that it is possible to estimate droplet dimensions in the gradient direction, even from an experimental setup that is only capable of visualization in the flow direction–vorticity plane. Many workers (26–30) have recently performed elegant flow-visualization experiments using elaborate experimental apparatus, some designed specially for viewing deformed droplets in the velocity gradient direction. Even without such equipment, droplet size in the gradient direction can be extracted by using simple volume conservation arguments.

How does the size of a droplet correlate with its location between the plates at steady state? As an example, data at

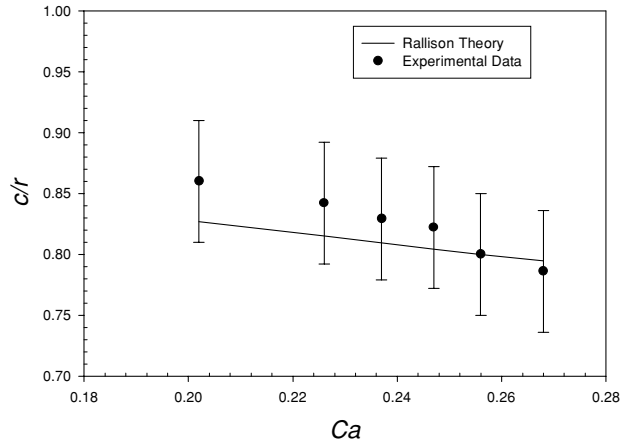


FIG. 4. Droplet dimension in the gradient direction (normalized by the quiescent droplet radius) for the 20% PDMS/PIB emulsion versus Ca . Points denote experimental data and the smooth curve denotes the prediction of the Rallison second-order theory. The bar on each data point reflects the standard uncertainty (standard deviation) associated with the point.

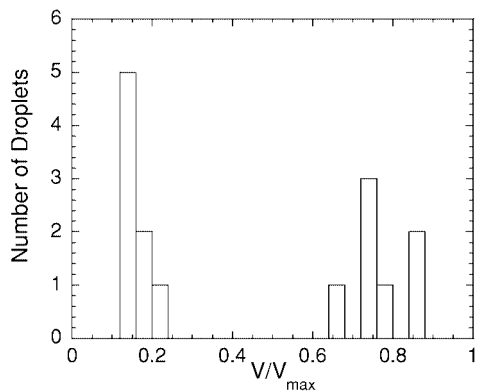


FIG. 5. Typical histogram showing velocity distribution of only those droplets whose size in the vorticity direction is less than half the mean size in the vorticity direction, in a 35% PDMS/PIB emulsion at $\dot{\gamma} = 4.5 \text{ s}^{-1}$.

$\dot{\gamma} = 4.5 \text{ s}^{-1}$ for a 35% PDMS/PIB emulsion were used to determine the droplet sizes and velocities. A histogram (see Fig. 5) was then prepared using the velocities of only “small” droplets, defined as those droplets whose size is less than half the average size in the vorticity direction. Small droplets are actually located closer to the walls than to the centerline, and there are almost no small droplets at the center. Larger droplets are preferentially located at the center, because, as we will discuss shortly, droplets migrate inward toward the centerline with a characteristic velocity which scales as r^4 . Smaller drops lie close to the wall, as during collisions with larger drops they are sent toward the wall. These results agree with the observations of King and Leighton (24), who also found that small drops are kept away from the centerline by larger drops. Figures 2 and 5 reveal a depletion zone (drop-free region) in the immediate vicinity of the confining walls, also reported by King and Leighton (24). This effect is due to both excluded volume and droplet migration effects. Excluded volume, of course, ensures that the distance between drop center and the wall (l) must exceed the drop radius, r . If $l > r$, wall migration effects will control the formation of the depletion region.

Composition Dependence

The overall effect of composition on droplet microstructure in general is shown in Fig. 6. The results for emulsions of various compositions are summarized in this morphology diagram, in the parameter space of mass fraction and shear rate. In concentrated blends (between 10 and 35% PDMS), we see a transition from two layers of droplets to one layer of droplets with decreasing $\dot{\gamma}$.

The formation of highly ordered pearl-necklace-like chains of particles (shaded data points in Fig. 6) is observed in the one layer state for emulsions containing 5 to 20% PDMS. Other data points in the one layer state (e.g., for 1% PDMS and 35% PDMS, which have not been shaded in Fig. 6), correspond to a disordered one layer microstructure. Data on the 5% PDMS emulsion at higher shear rates ($\dot{\gamma} = 8.5, 10.8, 13.3, 15.0,$ and 17.0 s^{-1} ; some data not shown in Fig. 6), show a disordered one layer microstructure; this system does not show a two-layer

state at any of the shear rates investigated. Optical micrographs of a 5% PDMS emulsion showing disordered microstructure at $\dot{\gamma} = 8.5 \text{ s}^{-1}$ and pearl-necklace arrangement at $\dot{\gamma} = 4.25 \text{ s}^{-1}$ are shown in Figs. 7a and 7b, respectively.

While Migler (4) had observed the formation of necklaces as a *transient* state during a study of the droplet-string transition kinetics for an emulsion containing 28% PDMS, we find here that the pearl-necklace morphology is a stable (nontransient) steady state at lower volume fractions, which persists for time scales on the order of several days without showing a transition to any other state. Although this is the first reported observation of pearl-necklace formation in suspensions where the dispersed phase is made of deformable fluid droplets, there have been related observations. Segré (31) reported the formation of necklace structures in hard-sphere suspensions flowing in tubes. Michele *et al.* (32) observed the alignment of hard-sphere suspensions subjected to oscillatory shear flow between parallel plates, with similar results reported by Petit and Noettinger (33) and Lyon *et al.* (34). In hard-sphere suspensions necklace formation has been observed when the matrix fluid is *viscoelastic*. In our system, the component fluids are Newtonian, with no measurable normal stresses. Further, while interfacial elasticity certainly contributes to normal stresses in an emulsion, our steady shear rheology experiments detect no measurable first normal stress difference in our emulsions over the shear rate range studied in the flow visualization experiments.

Finally, at the lowest shear rates, droplets in the one-layer state coalesce to form strings. Strings and droplets coexist at the lowest shear rate studied for each composition. A “dilute” (1% PDMS) emulsion did not form strings and only showed a single-layer disordered microstructure, due to the low concentration of droplets. The threshold shear rate at which strings first form

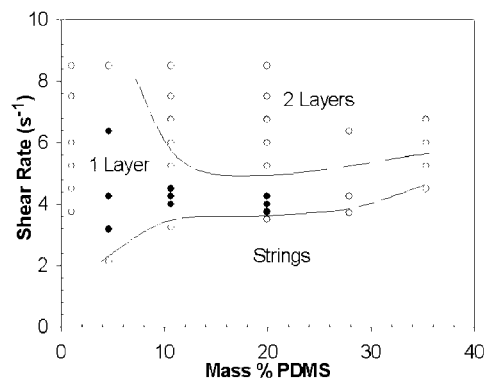


FIG. 6. Morphology diagram describing microstructure in confined PIB/PDMS emulsions, observed during *step-down* in shear (using the protocol described in Experimental), in the parameter space of mass fraction and shear rate, for a uniform gap-width ($36 \mu\text{m}$) and a fixed viscosity ratio ($\lambda = 1$). For each composition, experiments were started at 8.5 s^{-1} . Points denote shear rates where experimental data were obtained, and smooth curves are guides to the eye. Shaded points denote experimental observation of ordered pearl-necklace chains of droplets. The label “Strings” refers *only* to the experimental points along the curve where we first observed strings, and we discontinued our experiments there.

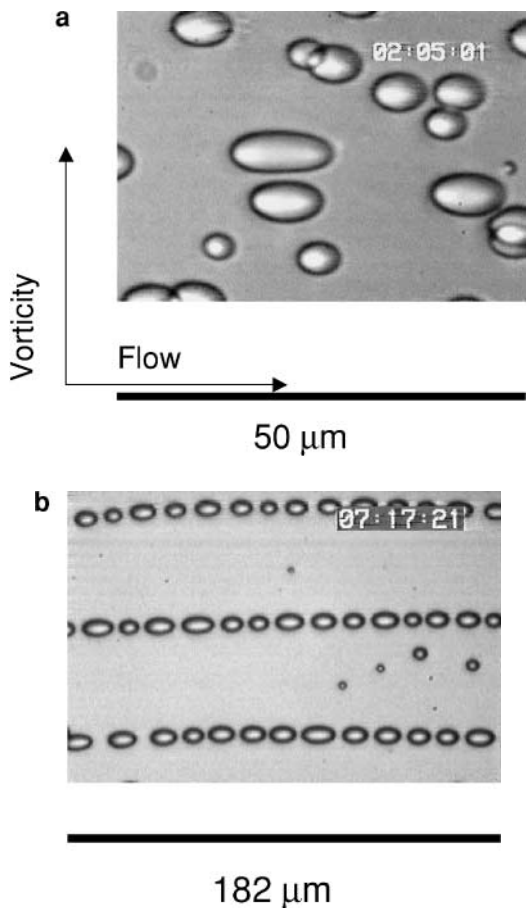


FIG. 7. Optical micrograph of a 5% PDMS/PIB emulsion: (a) at $\dot{\gamma} = 8.5 \text{ s}^{-1}$, showing disordered microstructure (note a pair of droplets colliding at the top of the figure and another at the bottom left edge), and (b) at $\dot{\gamma} = 4.25 \text{ s}^{-1}$, showing the pearl-necklace arrangement of PDMS droplets where collisions are essentially arrested. Vorticity and flow directions in each case are indicated by arrows.

in the system increases somewhat with increasing composition. This result may be understood qualitatively on the basis of an increase in droplet size and also in the increase in the number density of droplets with composition. Migler (4) has shown that the droplet-string transition occurs in the vicinity of $r/d \approx 0.5$. As the concentration of the droplet phase in the emulsion increases, this limiting r/d is attained at higher shear rates, leading to an increase in the threshold shear rate with composition. Finally, the position of phases (along the shear rate axis) in this morphology diagram is a function of the degree of confinement (r/d) imposed on the system. It is conceivable that the effect of decreasing the gap width would be to shift the boundary between the two-layer and one-layer states to higher shear rates, with similar effects on the threshold shear rate for string formation.

DISCUSSION

Interpretation of Layering Phenomenon

We begin with a brief discussion of the relevant transport phenomena that drive droplet motion in the velocity gradient di-

rection. When an emulsion is deformed under shear, the droplets drift away from bounding surfaces toward the centerline due to an “asymmetric disturbance velocity” (24). This effect, termed “wall migration,” was observed experimentally in emulsions by Mason *et al.* (35–37). Chaffey *et al.* (38, 39) proposed an analytical model that predicted droplet drift away from the walls in Couette flow. Another model, by Schowalter *et al.* (40), was found to reasonably describe the data of Smart and Leighton (41) on droplet migration in emulsions in Couette flow. Chan and Leal (42) derived the drift velocity of a droplet by accounting for the effect of both walls in a Couette flow and later (43) verified that their model showed reasonable agreement with experimental results. King and Leighton (24) determined that the results for droplet drift from single-drop experiments in a Couette cell were well described by the analytical solution of Chan and Leal (42). More recently, Imaeda (44) has provided a similar analytical expression. Droplet migration has also been studied extensively by Uijttewaai *et al.* (45, 46) and Kennedy *et al.* (47) using computer simulations.

Droplet collisions become important at higher concentrations of the dispersed phase and these collisions tend to cause droplet motion *perpendicular* to streamlines. Such collisions are *random* in uniform dispersions in the bulk and are thus equally likely to result in positive or negative displacements. This motion gives rise to droplet self-diffusion. However, the diffusivity is anisotropic, being greater in the velocity gradient direction than in the vorticity direction, as demonstrated by Loewenberg and Hinch (48) in their numerical simulation of binary droplet collisions in simple shear flow. They have also predicted that while the self-diffusion coefficient D_{self} is only a relatively moderate function of Ca it is a much stronger function of λ . Notably, this diffusion-like process in emulsions does *not* have origins in Brownian motion of drops, but in the random motions generated by flow. The Peclet number, $Pe = \frac{\dot{\gamma} r^2}{D_{\text{self}}} \approx \frac{\eta \dot{\gamma} r^3}{kT}$ (k and T denote Boltzmann’s constant and absolute temperature, respectively), is the ratio of flow effects to Brownian effects. For the flow situations here, $Pe \sim O(10^7)$, and hydrodynamic interactions are much more important than Brownian motion. Drift of droplets toward the centerline also sets up a concentration gradient, which is responsible for downgradient diffusion of droplets toward the wall in *bulk* systems. da Cunha and Hinch (49) have shown that the effective diffusion coefficient, D_{grad} describing downgradient diffusion exceeds D_{self} . King and Leighton (24), followed closely by Burkhart *et al.* (50), have argued that bulk systems at steady state have zero net droplet flux (diffusive and convective fluxes balance) and arrived at a parabolic steady state composition profile with a maximum at the centerline.

We had briefly alluded to the droplet composition profile earlier. While the experimental conditions in this work are certainly very different from those of the $r/d \ll 1$ case for which analytical composition profiles have been derived by King and Leighton (24) and by Burkhart *et al.* (50), we nevertheless quantitatively predict the droplet profile (using the model of Burkhart *et al.*) for the *bulk* case and compare it to the experimental distribution, purely for *qualitative* comparison purposes. The predictions of

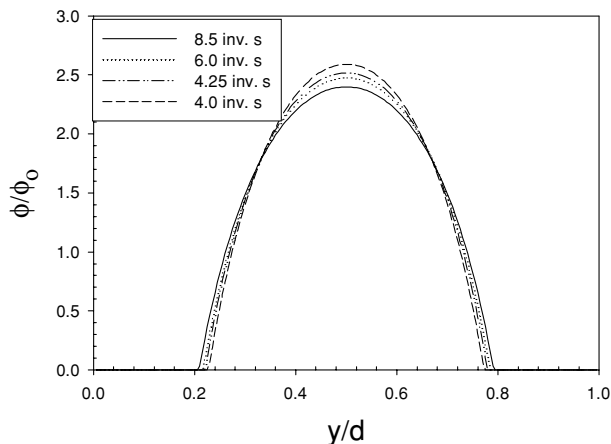


FIG. 8. Predictions of the model of Burkhart *et al.* (50) for the normalized volume fraction (ϕ/ϕ_0) profile (*bulk solution*) as a function of dimensionless distance y/d between the plates.

the volume fraction (ϕ) profile (see Fig. 8; compare to Fig. 2) are based on experimental r data on the 20% PDMS/PIB emulsion and assume a dimensionless gradient diffusivity = 0.16, which is four times greater than the dimensionless self-diffusivity. In Fig. 8 ϕ is normalized by the average volume fraction ϕ_0 . At $\dot{\gamma} = 8.5, 6.0,$ and 4.25 s^{-1} , the width of the parabolic composition profile is roughly comparable to the width of the velocity distribution. However, at $\dot{\gamma} = 4.0 \text{ s}^{-1}$, the velocity distribution is significantly narrower than the predicted composition profile, signifying the fact that confinement has quantitatively altered the composition profile. We will argue shortly that confinement accentuates the effect of wall migration and reduces collisions. The effective ϕ at the center of the gap between the plates ($y/h = 0.5$) increases with decreasing $\dot{\gamma}$, underscoring the importance of wall migration effects which send droplets to the center at lower $\dot{\gamma}$.

Molecular mass transfer due to concentration gradients (described by Fick's law of diffusion) results from *random* molecular motions, but when molecules are severely confined, their motion cannot be described in terms of Fickian diffusion (51). In analogy to the molecular case, due to severe confinement, droplet motion *in the velocity gradient direction* is not diffusive (as the droplets are too spatially constrained to exhibit diffusive motion). Due to the arrangement of the droplets in rather well-defined layers, gradient-induced diffusion may also be neglected. Diffusive motion of droplets may only be observed in the limit of bulk systems. Packing constraints imposed by finite-size effects can help us understand why it is not possible to fit more than one layer of drops when they become sufficiently large (relative to the gap width). However, for the two-layer state we need to understand what causes a spatial separation of droplets in the velocity gradient direction, and for the one-layer state we need to understand what causes the peak in the velocity distribution to appear roughly halfway between the plates. We therefore conjecture that droplet collisions (which can send droplet toward the walls) and wall migration (which sends droplets toward the

center) *may* be responsible for the formation of two droplets layers. We now substantiate our arguments by comparing the time scales relevant to droplet collisions and droplet migration.

We first estimate the number of collisions experienced by a droplet per unit time (collision frequency) from experimental data according to procedures outlined under Experimental. The collision frequency increases with shear rate (see Fig. 9), as expected, as the collisions are shear-induced. The bars on the data points reflect the standard uncertainty (standard deviation of the distribution) and are effectively a measure of the width of the distribution of the number of collisions suffered by the droplets in the ensemble. The number of collisions/unit time increases with increasing composition, when compared at any given shear rate, due to the increase in the number density of droplets with increasing volume fraction.

The classical von Smoluchowski (52) calculation of the collision frequency would seem to serve as the first choice to model the collision data. Assuming all drops are of equal size, the frequency with which one drop collides with another can be calculated easily. If the flow direction is taken to lie along the x axis, the velocity gradient along the y axis, and the test drop is placed at the origin, then the relative velocity of another drop at position y' is $\dot{\gamma} y'$. The total collision rate can be calculated as

$$C_0 = 2 \int_0^D 2 \int_0^{(D^2 - y^2)^{1/2}} \dot{\gamma} y' N(y, z) dz dy. \quad [3]$$

$N(y, z)$ is the number of drops per unit volume. While N may be a function of position for a structured (i.e., layered) emulsion,

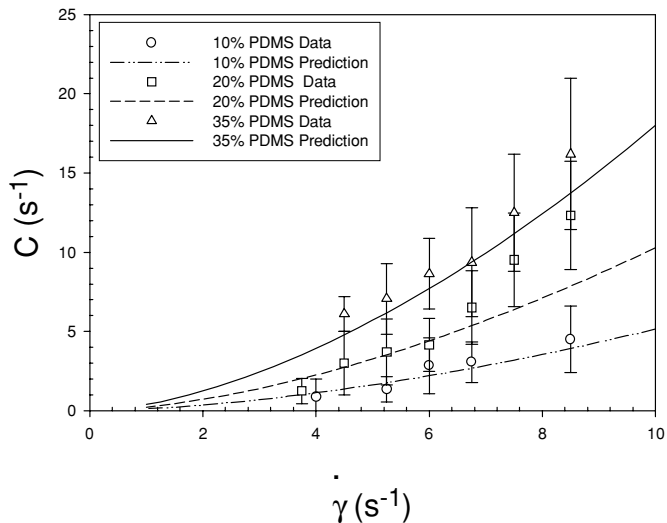


FIG. 9. Collision frequency, C , as a function of $\dot{\gamma}$ for droplets in PDMS/PIB blends of different compositions. Points denote experimental data, while curves denote predictions of Eq. [9]. The bar on each data point reflects the standard uncertainty (standard deviation) associated with the point.

it is uniform for a random (bulk) emulsion.

$$\bar{N}_{\text{bulk}} = \frac{6\phi}{\pi D^3}. \quad [4]$$

Here ϕ denotes the volume fraction of drops and D is the droplet diameter. In the bulk case, the collision rate C_0 reduces to the familiar expression.

$$C_0 = \frac{4}{3} \dot{\gamma} \bar{N} D^3 = \frac{8}{\pi} \dot{\gamma} \phi \quad [5]$$

In the layered state, the droplet concentration is nonuniform. In a two-layer state, $N(y, z)$ is asymmetric in y (remembering that we have assigned the origin to the center of the test drop). For example, if N is relatively large for positive y , it is nearly zero for negative y . To calculate N within the layered structure, we assume that wall migration (discussed shortly) has pushed all the drops into the central region of a given layer, causing an increase in the local concentration there. By volume conservation, the average number of drops per unit volume within each layer can be written thus.

$$\bar{N}_{2\text{-layer}} = \frac{3\phi d}{\pi D^4} \geq \bar{N}_{\text{bulk}} \quad [6]$$

The collision frequency is written as follows in the layered state.

$$C_{2\text{-layer}} = \int_0^D 2 \int_0^{(D^2-y^2)^{\frac{1}{2}}} \dot{\gamma} y' N(y, z) dz dy \quad [7]$$

The resulting collision frequency in the layered state is given by the following expression.

$$C_{2\text{-layer}} = \frac{1}{\pi} \dot{\gamma} \phi \frac{d}{r} \geq \frac{C_0}{2} \quad [8]$$

Since $r \leq d/4$, the minimum collision frequency of the two-layered state is half the bulk value, as a result of each droplet colliding with only droplets to one side. Considering that r depends on $\dot{\gamma}$, the collision frequency can be rewritten as

$$C_{2\text{-layer}} = \frac{1}{\pi} \dot{\gamma}^{1.6} \phi \frac{d}{R_1}, \quad [9]$$

where R_1 is a constant. The exponent on $\dot{\gamma}$ in Eq. [9] was written to be consistent with our experimental results. Different exponents are possible. When the Taylor stability criterion applies, the exponent on $\dot{\gamma}$ equals 2 and $R_1 = \frac{C_0 a_0 \sigma}{\eta_m}$. The layered state collision rate can be calculated more accurately, if a function more accurate than Eq. [6] were used to calculate $N(y, z)$. $N(y, z)$ is not uniform within the layer, as was assumed, but, in the layered state, has peaks at $y = 0$ and D . Since the integrand (Eq. 7) approaches zero at these values of y , the actual collision rate is less than that predicted by Eq. [8].

We evaluate R_1 from our data on $r(\dot{\gamma})$ for the 20% PDMS/PIB emulsion from the intercept of a plot of r vs $\dot{\gamma}$. Thus the only

unknown (R_1) in Eq. [9] is determined from the experimental data, and then Eq. [9] is used with *no adjustable parameters* to predict the collision frequency data in the layered state. The comparison between experimental data and the predictions of Eq. [9] is shown in Fig. 9. The model describes the experimental data well.

We now determine the time scale for droplet migration. Excluded volume effects ensure that droplets are found at least a distance c away from the wall. To form a one-layer system, the droplets would have to move *inward* (toward the centerline) from either layer and migrate a distance $O(c)$ in the velocity gradient direction. We calculate the time required for droplets to travel this distance. The motivation for this calculation is kinematical; if droplet centers lie within a distance c from the centerline, it is not possible to have two layers. We now calculate the drop migration velocity to determine the migration time.

We invoke the expression derived by Chan and Leal (42) for the droplet migration velocity, u_{mig} , for shear flow in narrow gap Couette geometry of a single deformable Newtonian drop in a Newtonian matrix (written here for the case $\lambda = 1$). This expression also applies to the motion of a droplet between two parallel plates, since the assumption of linear shear flow is well satisfied in the narrow gap limit. The shear rate is nearly uniform everywhere and is essentially the same as simple shear between two parallel plates.

$$u_{\text{mig}} = Ca\dot{\gamma}r \frac{r^2}{d^2} \frac{615}{256} \left[-y^* + \frac{1}{(1+2y^*)^2} - \frac{1}{(1-2y^*)^2} \right] \quad [10]$$

Here y^* is the coordinate describing the drop position between the plates, centered in the middle of the gap between the two plates, and rendered dimensionless with the gap width d : $y^* \in [-0.5, 0.5]$. While u_{mig} vanishes at the center ($y^* = 0$), it diverges at the walls ($y^* = \pm 0.5$).

In support of our conjecture that the interplay between droplet collisions and wall migration may be responsible for the formation of droplet layers, we compare the migration time scale, t_{mig} , with the average time elapsed between droplet collisions, t_{coll} . Both time scales were calculated using experimental data on r for the 20% PDMS/PIB emulsion. The time scale t_{coll} was calculated as the inverse of $C_{2\text{-layer}}$ (which is calculated from Eq. 9), while t_{mig} was calculated as $t_{\text{mig}} = \int \frac{dy}{u_{\text{mig}}}$ (see Fig. 10). As discussed earlier, the limits of this integral are dictated by the excluded volume condition that the droplets must lie a distance c away from the wall and also by the condition that the drops should move through a distance c in the velocity gradient direction. The ratio $T = \frac{t_{\text{coll}}}{t_{\text{mig}}}$ increases and approaches unity with decreasing $\dot{\gamma}$. When $T < 1$, collisions occur faster than migration, displacing droplets in the velocity gradient direction and the two-layer microstructure results. When $T \sim O(1)$, collision and migration occur on similar time scales, causing accumulation of droplets in one layer.

The dependence of T on $\dot{\gamma}$ can be understood by remembering that r depends on $\dot{\gamma}$. We can easily discern from Eq. [8] that $t_{\text{coll}} \sim r/\dot{\gamma}\phi$. Similarly, using Eq. [10], we derive $t_{\text{mig}} \sim r^{-3}\dot{\gamma}^{-2}$.

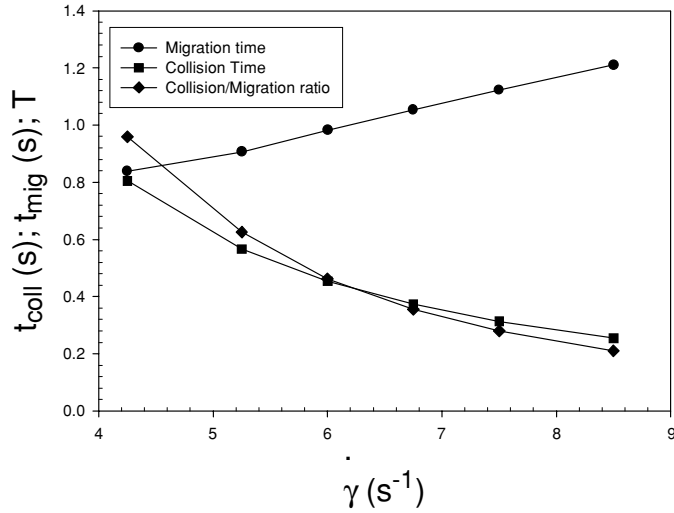


FIG. 10. Calculated time scale between collisions, t_{coll} , (calculated from collision frequency model) and calculated time scale, t_{mig} , for drops to migrate a distance $O(c)$ inward from the wall (calculated using migration velocity) plotted as a function of $\dot{\gamma}$. The ratio of these two quantities is also plotted versus $\dot{\gamma}$. All calculations have been performed for the 20% PDMS/PIB system. All lines merely serve to guide the eye.

Using these two scaling relationships, we get $T \sim r^4 \dot{\gamma} \phi^{-1} \sim \dot{\gamma}^{-3} \phi^{-1}$ (by using the Taylor relation $r \sim \dot{\gamma}^{-1.0}$). From these simple scaling arguments, we see that T increases with decreasing $\dot{\gamma}$, signifying that migration gains importance relative to collision upon decreasing $\dot{\gamma}$. This is the basis of our argument that when t_{coll} and t_{mig} are comparable, the two-layer state shows a transition to the one-layer state, leading us to anticipate that the ratio T is a relevant dimensionless quantity in defining the nature of the confined state of an emulsion. Note from Eq. [9] that $t_{\text{coll}} \sim \phi^{-1}$, so that $T \sim \dot{\gamma}^{-3} \phi^{-1}$. Mapping $T \approx 1$ yields a curve that approximately tracks the boundary between the one-layer and two-layer states.

We also evaluate T for the system of Zhou and Pozrikidis (22). From the information in their paper, we discern $r/d = 1/8$. From Eq. [8], we calculate a collision frequency $C_0 = \frac{1}{\pi} \dot{\gamma} \phi \frac{d}{r} = \frac{8}{\pi} \dot{\gamma} \phi$ in the two-layer state (since $r/d = \frac{1}{8}$) and from Eq. [10] the migration time scale as $\frac{u_{\text{mig}}}{r} (y^* = 0.125) = Ca \dot{\gamma} \frac{r^2}{d^2} \frac{615}{256} = 1 \dot{\gamma} \frac{1}{8^3} \frac{615}{256} [\frac{1}{8}]$. The ratio of these collision and migration time scales is $T = \dot{\gamma} \frac{1}{8^3} \frac{615}{256} \div \frac{8}{\pi} \dot{\gamma} \phi$ ($Ca=1$ and $\lambda=1$; see Section III.A in Ref. 22). If we consider a length $L = 2H$, where $2H$ is the channel width (see Fig. 1 in Ref. 22), then we calculate a local $\phi = \frac{\pi a^2}{4H^2} = \frac{\pi}{4} \frac{1}{4^2} \cong 0.05$ ($a/H = 1/4$). This gives $T = 0.038 \ll 1$. By our criterion, we expect the two-layer state to be stable, in agreement with the simulation results of Zhou and Pozrikidis (22) for perturbations to the one-layer state, where the drops are displaced by a distance $\xi = r$ or $2r$ in “an alternating fashion across the centerline of the channel.”

Role of Body and Surface Forces

Since the densities of PIB and PDMS are not exactly matched, PDMS droplets will show some Stokes sedimentation. Is Stokes

sedimentation significant in this problem? We also ask how buoyancy effects and interfacial-tension-driven effects compare with each other.

The Bond number, Bo , gives the ratio of hydrostatic pressure relative to interfacial tension effects: $Bo = \frac{\Delta \rho g r^2}{\sigma}$, where $\Delta \rho$ is the difference between component densities and g is the acceleration due to gravity. Assuming an average $r \sim O(20 \mu\text{m})$, we get $Bo \sim O(10^{-4})$, and we conclude that interfacial tension effects dominate buoyancy effects.

We compare Stokes sedimentation to wall migration effects by evaluating the ratio of the droplet migration velocity to the buoyancy-driven velocity (53), u_{buoy} , calculated independently by Hadamard (54) and Rybczynski (55). When a droplet reaches this velocity, by definition, the sum of the viscous retarding (Stokes drag) force and the buoyancy force equals the weight of the droplet (assumed spherical).

$$u_{\text{buoy}} = \frac{2(\rho_d - \rho_m)g}{9} \frac{\lambda + 1}{\eta_m} \frac{r^2}{\lambda + \frac{2}{3}} \quad [11]$$

The ratio of u_{buoy} and u_{mig} is used to calculate the relative contributions of buoyancy and migration to the movement of drops away from the top wall, written here for $\lambda = 1$. We use a linearized form of u_{mig} here: $u_{\text{mig}} = -\frac{5535}{256} Ca \frac{r^2}{d^2} r \dot{\gamma} y^*$.

$$\frac{u_{\text{mig}}}{u_{\text{buoy}}} = \frac{249075}{3072} Ca \frac{r \dot{\gamma}}{d^2} \frac{\eta_m}{\Delta \rho g} y^* \quad [12]$$

We set $y^* = 0.1$ (where the linearization of u_{mig} is reasonable) above, and find that u_{mig} exceeds u_{buoy} by a factor $O(10^4)$. For droplets close to the top plate (wall migration and buoyancy act in the same direction for them), inward motion is controlled by wall migration effects. For droplets close to the bottom plate (where buoyancy and wall migration act in opposing directions), migration effects are far stronger than buoyancy effects. Alternatively, we can also determine the y^* where u_{mig} and u_{buoy} become equal. In the 20% PDMS emulsion, at $\dot{\gamma} = 8.5 \text{ s}^{-1}$ ($r = 7.8 \mu\text{m}$ and $Ca = 0.26$), we find that this value of y^* is 7×10^{-5} . Buoyancy and migration effects become comparable *near the centerline only*, and wall migration clearly dominates Stokes sedimentation elsewhere.

Finally we consider surface forces relevant to this problem. Stone and Kim (2) have alluded to the potential importance of surface phenomena in microfluidic and nanofluidic flows. What role do wetting and surface effects play in this problem, if any? The surface energies of quartz, PIB, and PDMS are 50×10^{-3} , 33.6×10^{-3} , and $20 \times 10^{-3} \text{ N/m}$, respectively (56). Since PDMS has a surface energy lower than that of PIB, it will preferentially wet the quartz substrate. Does this preferential wetting play any role in the problem?

To quantify the van der Waals interactions between the PDMS droplets (suspended in the PIB matrix) and the quartz substrate, we calculate the Hamaker constant A_{TOTAL} , as suggested by Israelachvili (56). He has provided the expression for A_{TOTAL} ,

describing the van der Waals interaction between a droplet of species “1” in medium “3” with the surface of medium “2.”

$$A_{\text{TOTAL}} \approx \frac{3}{4}kT \left(\frac{\varepsilon_1 - \varepsilon_3}{\varepsilon_1 + \varepsilon_3} \right) \left(\frac{\varepsilon_2 - \varepsilon_3}{\varepsilon_2 + \varepsilon_3} \right) + \frac{3h\tilde{\nu}_e}{8\sqrt{2}} \times \frac{(v_1^2 - v_3^2)(v_2^2 - v_3^2)}{(v_1^2 + v_3^2)^{\frac{1}{2}}(v_2^2 + v_3^2)^{\frac{1}{2}} \{ (v_1^2 + v_3^2)^{\frac{1}{2}} + (v_2^2 + v_3^2)^{\frac{1}{2}} \}} \quad [13]$$

Here ε_i denotes the dielectric constant of phase i , $\tilde{\nu}_e$ is the main electronic absorption frequency in the UV ($3 \times 10^{-15} \text{ s}^{-1}$), h is Planck’s constant ($6.626 \times 10^{-34} \text{ J} \cdot \text{s}$), and v_i is the refractive index of medium i . We are interested in calculating the van der Waals interaction between a droplet of species 1 (PDMS) in PIB (medium 3) with the surface of quartz (medium 2). Using the permittivities and refractive indices of glass, PIB, and PDMS, we determine that A_{TOTAL} for this case is $2.2 \times 10^{-21} \text{ J}$. Since $A_{\text{TOTAL}} > 0$, there is attraction between the PDMS droplet and the surface, albeit a weak one. In the phase-inverted situation where PIB is the droplet phase (1) suspended in a PDMS matrix (3) interacting with quartz surface (2), A_{TOTAL} is even smaller ($1.5 \times 10^{-21} \text{ J}$), but still attractive. This smaller value of A_{TOTAL} is *consistent* with the wetting scenario: PDMS prefers to wet the quartz walls over PIB. While van der Waals forces are long-range forces, they are weak and their effect is expected to be negligible over length scales on the order of the distance between the droplets and the quartz walls. The separation between the walls and the PDMS droplets is at least a few micrometers (wall migration effects are strongest near the wall and our data show that there are *no droplets* immediately adjacent to the wall). Since van der Waals forces are important at submicrometer length scales (typically $\leq 0.01 \mu\text{m}$, Ref. 56), we conclude that surface phenomena have a negligible role here. Fluid mechanics effects such as wall migration and droplet collisions overwhelm the (relatively) small surface effects. It is conceivable that surface phenomena would become significant in this problem if we were operating in the nanofluidic regime, however.

SUMMARY

We have studied droplet microstructure in emulsions sheared under conditions where the average droplet size is of the order of the separation between the confining surfaces. Finite-size effects result in phenomena quite distinct from those observed in the bulk. We find that the droplets organize themselves into layers in confined emulsions sheared between parallel plates. The number of layers that can be formed at any given shear rate is a function of finite-size effects as well as two other well-known effects in emulsion rheology: migration of droplets from the walls toward the center and droplet collisions. We have argued why the two-layer state may be stable under some conditions, by comparing the time scales germane to droplet migration and droplet collisions. While we have offered some simple arguments to attempt

the rationalization of our experimental observations, we stress that the physics behind the formation of the layered morphology is indeed poorly understood. It is our hope that these results will stimulate some theoretical attempts to probe the underpinnings of this phenomenon. We have also seen that the arrangement of droplets in necklace-like chains in the one-layer state is a stable morphology. The droplet microstructure in the droplet-string transition is a function of composition, and we have summarized the results of a composition dependence study in the form of a rich morphology diagram in the parameter space of composition and shear rate. Current work is focused on exploring the elasticity and viscosity ratio effects on the microstructure in these confined emulsions, which will be reported in a subsequent publication.

ACKNOWLEDGMENTS

M.C.D. was kindly supported by the NIST Summer Undergraduate Research Fellowship Program. We thank Kathy Flynn for assistance with video data analysis. Helpful discussions with Jack Douglas, Edmund DiMarzio, and Patricia McGuiggan (NIST) are gratefully acknowledged. We especially thank David Leighton, Jr. (Univ. of Notre Dame), and Jack Douglas for insightful criticisms of the manuscript. We also thank Erik Hobbie, David vanderHart, and Nikos Martys (NIST) for a critical reading of the manuscript. Finally, we also thank the two referees for their extremely helpful comments.

REFERENCES

- Happel, J., and Brenner, H., “Low Reynolds Number Hydrodynamics” Nijhoff, The Hague, 1983.
- Stone, H. A., and Kim, S., *AIChE J.* **47**, 1250–1254 (2001).
- Whitesides, G. M., and Stroock, A. D., *Phys. Today* **June** 42–48 (2001).
- Migler, K. B., *Phys. Rev. Lett.* **86**, 1023–1026 (2001).
- Taylor, G. I., *Proc. R. Soc. London A* **138**, 41–48 (1932).
- Taylor, G. I., *Proc. R. Soc. London. A* **146**, 501–523 (1934).
- Grace, H. P., *Chem. Eng. Commun.* **14**, 225–277 (1982).
- Rallison, J. M., *Annu. Rev. Fluid Mech.* **16**, 45–66 (1984).
- Stone, H. A., *Annu. Rev. Fluid Mech.* **26**, 65–102 (1994).
- Chesters, A. K., *Trans. I. Chem. E.* **69**, 259–270 (1991).
- Yang, H., Park, C. C., Hu, Y. T., and Leal, L. G., *Phys. Fluids* **13**, 1087–1106 (2001).
- Mason, T. G., *Curr. Opinion Colloid Interface Sci.* **4**, 231–238 (1999).
- Ackerson, B. J., and Pusey, P., *Phys. Rev. Lett.* **61**, 1033–1036 (1988).
- Ackerson, B. J., *J. Rheol.* **34**, 553–590 (1990).
- Doi, M., *J. Chem. Phys.* **79**, 5080–5087 (1983).
- Kowalewski, T. A., *Exp. Fluids* **2**, 213–219 (1984).
- Hiller, W., and Kowalewski, T. A., *Exp. Fluids* **5**, 43–48 (1987).
- Fetters, L. J., Lohse, D. J., and Colby, R. H., in “Physical Properties of Polymers Handbook” (J. E., Mark, Ed.), Chap. 24. AIP Press, Woodbury, NY 1996.
- Minale, M., Moldenaers, P., and Mewis, J., *Macromolecules* **30**, 5470–5475 (1997).
- Wagner, M., and Wolf, B. A., *Macromolecules* **26**, 6498–6502 (1993).
- Eckstein, E. C., Bailey, D. G., and Shapiro, A. H., *J. Fluid Mech.* **79**, 191–208 (1977).
- Zhou, H., and Pozrikidis, C., *Phys. Fluids A* **5**, 311–324 (1993).
- Karnis, A., Goldsmith, H. L., and Mason, S. G., *J. Colloid Interface Sci.* **22**, 531–553 (1966).
- King, M. R., and Leighton, D. T., *Phys. Fluids* **13**, 397–406 (2001).
- Rallison, J. M., *J. Fluid Mech.* **98**, 625–633 (1980).
- Guido, S., and Greco, F., *Rheol. Acta* **40**, 176–184 (2001).

27. Levitt, L., Macosko, C. W., and Pearson, S. D., *Polym. Eng. Sci.* **36**, 1647–1655 (1996).
28. Guido, S., and Villone, M., *J. Rheol.* **42**, 395–415 (1998).
29. Mighri, F., Carreau, P. J., and Ajji, A., *J. Rheol.* **42**, 1477–1490 (1998).
30. Guido, S., Greco, F., and Villone, M., *J. Colloid Interface Sci.* **219**, 298–309 (1999).
31. Segre, G., “Proceedings of the Fourth International Congress of Rheology.” Part 4, “Symposium on Biorheology,” pp. 103–118, Wiley Interscience, 1963.
32. Michele, J., Pätzold, R., and Donis, R., *Rheol. Acta* **16**, 317–321 (1977).
33. Petit, L., and Noetinger, B., *Rheol. Acta* **27**, 437–441 (1988).
34. Lyon, M. K., Mead, D. W., Elliott, R. E., and Leal, L. G., *J. Rheol.* **45**, 881–890 (2001).
35. Goldsmith, H. L., and Mason, S. G., *J. Colloid Sci.* **17**, 448–476 (1962).
36. Karnis, A., and Mason, S. G., *J. Colloid Interface Sci.* **24**, 164–169 (1967).
37. Goldsmith, H. L., and Mason, S. G., in “Rheology: Theory and Applications” (F. R. Eirich, Ed.), Chap. 2. Academic Press, New York, 1967.
38. Chaffey, C. E., Brenner, H., and Mason, S. G., *Rheol. Acta* **4**, 64–72 (1965).
39. Chaffey, C. E., Brenner, H., and Mason, S. G., *Rheol. Acta* **6**, 100 (1967).
40. Schowalter, W. R., Chaffey, C. E., and Brenner, H., *J. Colloid Interface Sci.* **26**, 152–160 (1968).
41. Smart, J. R., and Leighton, D. T., *Phys. Fluids A* **3**, 21–28 (1991).
42. Chan, P. C.-H., and Leal, L. G., *J. Fluid Mech.* **92**, 131–170 (1979).
43. Chan, P. C.-H., and Leal, L. G., *Int. J. Multiphase Flow* **7**, 83–99 (1981).
44. Imaeda, T., *Phys. A* **285**, 306–314 (2000).
45. Uijttewaal, W. S. J., Nijhof, E.-J., and Heethaar, R. M., *Phys. Fluids A* **5**, 819–825 (1993).
46. Uijttewaal, W. S. J., and Nijhof, E.-J., *J. Fluid Mech.* **302**, 45–63 (1995).
47. Kennedy, M. R., Pozrikidis, C., and Skalak, R., *Comp. Fluids* **23**, 251–278 (1994).
48. Loewenberg, M., and Hinch, E. J., *J. Fluid Mech.* **338**, 299–315 (1997).
49. da Cunha, F. R., and Hinch, E. J., *J. Fluid Mech.* **309**, 211–223 (1996).
50. Burkhart, B. E., et al., *Phys. Rev. Lett.* **87**, 98304–98308 (2001).
51. Welty, J. R., Wicks, C. E., and Wilson, R. E., “Fundamentals of Momentum, Heat and Mass Transfer.” Wiley & Sons, New York, 1984.
52. von Smoluchowski, M., *Z. Phys. Chem.* **92**, 129–168 (1917).
53. Lamb, H., “Hydrodynamics,” 6th ed. Dover, New York, 1932.
54. Hadamard, M. J., *C. R. Acad. Sci.* **152**, 1735–1738 (1911).
55. Rybczynski, W., *Bull. Int. Acad. Cracovice Ser. A: Sci. Math.* 40–46 (1911).
56. Israelachvili, J., “Intermolecular and Surface Forces,” 2nd ed. Academic Press, New York, 1991.